Research articles

Quantitative imaging of the magnetic field distribution in an artificial spin ice studied by off-axis electron holography

Teresa Weßels [a,b,*], András Kovács [a,*], Sebastian Gliga [c], Simone Finizio [c], Jan Caron [a], Rafal E. Dunin-Borkowski [a]

[a] *Ernst Ruska-Centre for Microscopy and Spectroscopy with Electrons and Peter Grünberg Institute, Forschungszentrum Jülich, 52425 Jülich, Germany*
[b] *Lehrstuhl für Experimentalphysik IV E, RWTH Aachen University, 52056 Aachen, Germany*
[c] *Swiss Light Source, Paul Scherrer Institut, 5232 Villigen PSI, Switzerland*

ARTICLE INFO

ABSTRACT

The magnetic state, including the stray fields, of a chiral pattern of interacting permalloy nanomagnets is studied using off-axis electron holography in the transmission electron microscope. The projected in-plane magnetisation of the nanomagnets is reconstructed from the experimental magnetic phase shift using model-based iterative reconstruction. The thickness and chemical composition of the nanomagnets are characterised in cross-sectional geometry. The average value of the magnetic polarisation of the permalloy through the thickness of the sample is measured to be 0.73 T. This value is lower than the bulk value of 1 T, likely as a result of a combination of the microstructure, composition and possible oxidation of the nanomagnets. The experimental results are compared to micromagnetic simulations to confirm the magnetic states and to understand the switching processes in the magnetic nanoislands.

1. Introduction

Artificial spin ices have received growing experimental and theoretical attention owing to their unique physics based on frustration [1,2], as well as their promising potential for magnonic [3,4] and logic devices [5,6]. Artificial spin ices consist of regular geometrically-arranged soft ferromagnetic nanoislands, in which the magnetisation points in one of two orientations along the long axes of the magnets due to shape anisotropy [7]. Here, we study a 'chiral ice' [8,9], whose geometry is such that it cannot be superimposed onto its mirror image when considering the edges of the array. It was recently demonstrated that spin ices with this geometry display chiral dynamics during magnetic-field-induced reversal [10], as well as during thermal relaxation, thus enabling the realisation of an active material with ratchet behaviour [8]. These dynamics were attributed to the details of the magnetisation distribution and to the topology of the magnetostatic field generated at the edges of the lattice, highlighting the importance of simultaneously measuring the stray field distribution and the magnetisation state in such systems.

Over the past years, a number of magnetic characterisation techniques have been used to image artificial spin ices, including magnetic force microscopy [11], SQUID-on-tip [10] and photoemission electron microscopy combined with X-ray magnetic circular dichroism as a contrast mechanism [12,13]. Alternatively, the magnetic fields generated

by individual ferromagnetic islands can be mapped using transmission electron microscopy (TEM) methods, including differential phase contrast imaging [14] and off-axis electron holography [15], which provide high spatial resolution and sensitivity to in-plane magnetic field components. The advantages and applications of these techniques are described in Ref. [16].

In this work, off-axis electron holography in the TEM is applied to study the magnetic state and magnetic field distribution in a chiral spin ice. The basic considerations of measuring the magnetic phase shift and recovering the in-plane magnetic polarisation are first presented. Experimental results on the characteristic magnetic state and magnetisation reversal mechanism in the nanoislands are then analysed, with the support of micromagnetic simulations. A complete quantitative reconstruction of both the in-plane magnetic induction and the magnetic polarisation of the nanomagnets in the chiral ice are presented.

2. Materials and methods

Chiral spin ice samples were prepared using electron beam lithography [17]. A permalloy (Py) nanomagnet pattern was deposited by thermal deposition of $Ni_{83}Fe_{17}$ onto a 100 μm × 100 μm large 20-nm-thick SiN membrane supported on a Si chip. The individual nanomagnets were designed to have dimensions of 470 nm × 170 nm ×

10 nm (length × width × thickness), with a centre-to-centre distance of 420 nm. Thin Cr layers were deposited below and on top of the patterned structure using thermal evaporation, in order to increase the adhesion of the Py to the membrane and to protect the structures from oxidation. In order to reduce electron-beam-induced charging of the SiN during off-axis electron holography experiments, a thin (<10 nm) Al layer was deposited over the whole sample. The thickness of each layer was verified during deposition by means of a quartz balance.

The thickness and chemical composition of the patterned islands were measured from a cross-sectional specimen prepared in a dual beam focused ion beam (FIB) scanning electron microscopy (SEM) system (Thermo Fisher Scientific Helios Nanolab 460f1). A section was first cut from the membrane samples and transferred to a Si substrate. Conventional lift-out was then used to prepare an electron-transparent lamella, which was attached to a standard Cu Omniprobe-style support grid. Analytical measurements were carried out using energy dispersive X-ray spectroscopy (EDS) and high-angle angular dark-field (HAADF) scanning TEM (STEM) in a probe aberration corrected TEM [18] operated at 200 kV (Thermo Fisher Scientific Titan 80-200) equipped with an in-column EDS detector (Super-X, ChemiSTEM technology). Spectrum images were recorded and processed using Velox software (Thermo Fisher Scientific). The chemical composition was determined using a conventional Cliff-Lorimer approach. Magnetic imaging [19, 20] studies were carried out in magnetic-field-free conditions (Lorentz mode) using an image aberration corrected TEM [21] operated at 300 kV (Thermo Fisher Scientific Titan 60-300). Fresnel defocus images and off-axis electron holograms were recorded using a direct electron counting detector [22] (Ametek (Gatan) K2 IS) and a single electron biprism positioned close to one of the conjugate image planes of the electron optical system. A modified tomography specimen holder [23] was used to control the sample inside the electron microscope. Data processing was performed with home-written Python scripts [24,25].

3. Theoretical background

Transmission electron microscopy utilises different signals resulting from the electron-sample interaction process to image the microstructure, chemical composition, electronic structure and electromagnetic fields of materials. De Broglie postulated in 1924 that electrons can be treated as quanta of the electron wave with momentum $\mathbf{p} = m\mathbf{v} = \hbar\mathbf{k}$, where m is the relativistic mass of an electron and $\mathbf{k}$ is the wave vector. The magnitude of the wave vector is related to the wavelength λ of the electron wave via $|k| = 1/\lambda$. Thus, a relativistic momentum p can be attributed to electrons with $p = h/\lambda$.

The Schrödinger equation describes a non-relativistic wave equation for a wave function ψ in the form

$$\left[\frac{1}{2m_0}(-i\hbar\nabla + e\mathbf{A})^2 - eV\right]\psi = E\psi \ , \tag{1}$$

where m_0 is the electron rest mass, $\mathbf{A}$ is the magnetic vector potential, V is the electrostatic potential and E is the total energy. For relativistic electrons, the wave vector can be approached through the Klein–Gordon equation. Lengthy details of paraxial wave dynamics based on quantum mechanics that describe electron wave propagation and interaction with matter are described in Ref. [26].

An analytical solution for the electron wave function gives the Aharonov–Bohm phase shift, which can be written in the form

$$\varphi(\mathbf{r}, z) = \varphi_0 - C_E \int_{z_0}^{z} dz' V_{el}(\mathbf{r}, z') + \frac{\pi}{\Phi_0} \int_{z_0}^{z} dz' A_z(\mathbf{r}, z') \ , \tag{2}$$

where φ_0 is the phase shift of an electron wave travelling through vacuum, while the second and third terms represent the contributions of electrostatic and magnetic phase shifts, respectively. The phase shift of an electron by an enclosed magnetic flux, without interaction with the magnetic induction $\mathbf{B}$ field, was predicted by Aharonov and Bohm [27] and earlier by Ehrenberg and Siday [28]. The prefactor $C_E = \frac{e\gamma m_0}{\hbar^2 k}$ is

a constant that depends on the wavelength of the electron wave. The term $\Phi_0 = \frac{\pi\hbar}{e} = 2.068 \cdot 10^{-15}$ is a magnetic flux quantum in Webers [Wb]. Only components of the magnetic induction field perpendicular to the electron beam direction can be measured.

Stokes' theorem can be used to show that the magnetic flux Φ_M is embraced by a loop of the different paths that an electron travels around the in-plane component of the magnetic field. The corresponding magnetic phase shift is

$$\delta\varphi_{mag} = -2\pi\frac{e}{h}\Phi_M \ . \tag{3}$$

It is important to note that the magnetic phase shift $\delta\varphi_{mag}$ does not provide any means to measure the magnetic vector potential. In general, as the electron wave propagates through a $\mathbf{B}$ field, it experiences a Lorentz force. A phase shift is induced, which is given by the enclosed magnetic flux integrated along the electron beam direction. Detailed analysis shows that $\nabla\varphi_{mag}(x, y)\mathbf{B}_{proj}(x, y) = 0$. Based on the assumption that the magnetic field does not vary in the electron beam direction, magnetic flux lines can be visualised in the form of contour lines, as the phase lines then agree with $\mathbf{B}_{proj}(x, y)$ according to the expression

$$\frac{d\varphi(x)}{dx} = \frac{et}{\hbar}B_{proj}(x) \ . \tag{4}$$

Eq. (2) describes how an electron phase shift measurement provides information about electrostatic and magnetic fields within and around a sample. In contrast to standard TEM imaging, phase information can be recovered using off-axis electron holography [29]. The technique is based on the interference of two parts of an electron wave. Fig. 1(a) shows a schematic image of the electron pathway for off-axis electron holography and the main elements of a TEM. Off-axis electron holography relies on the overlap of an electron wave that travelled through vacuum (reference wave) with one that passed through the sample (object wave). Interference is achieved by using an electron biprism that is inserted close to a conjugate image plane of the electron microscope lens system. Details of off-axis electron holography experiments and of the reconstruction steps can be found in Refs. [19,20,29].

All phase contrast techniques in the TEM are only sensitive to the in-plane components of the magnetic induction. Inside the specimen, $\mathbf{B} = \mu_0(\mathbf{H} + \mathbf{M})$, where μ_0 is the vacuum permeability, $\mathbf{M}$ is the magnetisation and $\mathbf{H}$ is the demagnetising field, whereas outside the specimen the magnetic induction is equal to the stray field. Normally, only a measurement of the projected in-plane components of the $\mathbf{B}$ field is possible and information about the magnetisation is not directly accessible. The magnetic moment of an isolated object, such as a nanocrystal, can be measured quantitatively by integrating the gradient of the phase around it using a circular integration contour [30]. This approach is model-independent, meaning that it does not rely on assumptions such as uniformity of the magnetisation in the particle or *a priori* knowledge such as the particle's morphology and/or composition. Alternatively, a model-based iterative reconstruction (MBIR) method can be used [25], in order to allow the projected in-plane magnetisation to be determined from a magnetic phase image recorded using off-axis electron holography [19,31]. The magnetisation is encoded in a phase image in the form

$$\varphi_{mag}(x, y) = -\frac{\mu_0}{2\Phi_0} \int \frac{(y - y') \cdot M_x - (x - x') \cdot M_y}{(x - x')^2 + (y - y')^2} dx' dy' \ . \tag{5}$$

Eq. (5) describes the forward problem of calculating a magnetic phase image from a given in-plane magnetisation distribution. The inverse problem of retrieving the projected in-plane magnetisation distribution from a measured magnetic phase image is ill-posed, *i.e.*, a solution for the magnetisation $\mathbf{M}_{x,y}$ may not exist, or, if it does, it may not be unique. The inverse problem can be solved by applying a MBIR algorithm. In a first step, the ill-posed problem is approximated by a least squares minimisation, which guarantees the existence of a solution. In order to enforce the uniqueness of the solution, Tikhonov
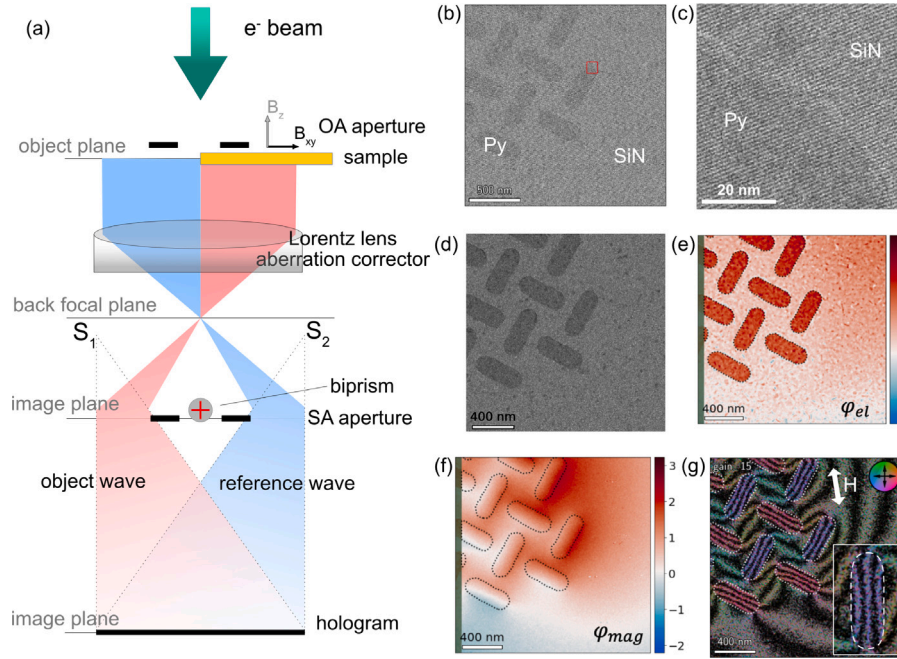
Fig. 1. (a) Schematic image of the electron optical parts and electron wave paths in off-electron holography in the TEM. The electron optical configuration is equivalent to the use of two electron sources S_1 and S_2 to form a hologram in the image plane. (b) Off-axis electron hologram of a corner of the Py chiral ice sample deposited on a SiN support layer. The enlarged region in (c) shows the holographic interference fringes. (d) Amplitude image reconstructed from the hologram. (e) Electrostatic φ_{el} and (f) magnetic φ_{mag} contributions to the phase shift recorded from the Py islands. The colour coding is in units of radians. (g) Magnetic induction map. The contour spacing corresponds to $2\pi/15$ rad. The arrow indicates the direction of the magnetic field H that was used to magnetise the sample. The inset shows a magnified view of a Py island. The induction lines curl slightly at the ends of the islands, resulting in S-shaped distributions.
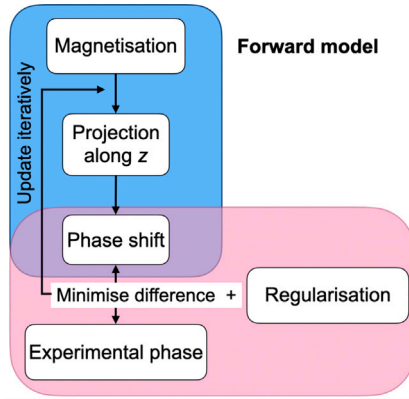

Fig. 2. Simplified steps of model-based iterative reconstruction of the magnetisation. The phase shift simulated for a given magnetisation distribution is compared to an experimentally-measured phase map. An iterative approach involving regularisation is used to improve the fitted magnetisation distribution.

regularisation of first order is employed to apply a smoothness constraint to the reconstructed magnetisation distribution. This approach is motivated by minimisation of the exchange energy of the system [32], ensuring that the solution represents a physically meaningful magnetisation distribution. The strength of the exchange interaction can be set in the form of a regularisation parameter. Fig. 2 shows the processing steps for the complete minimisation process, including the use of a forward model to reconstruct the projected in-plane magnetisation. This approach can be further extended to retrieve the three-dimensional magnetisation distribution from measurements of phase shift recorded while tilting the specimen. A full description of the MBIR procedure is described in Ref. [25].

4. Results

Quantitative magnetic imaging requires a knowledge of the thickness and composition of the measured Py elements. This information was obtained from a cross-sectional specimen prepared using focused ion beam milling. Fig. 3 shows a cross-sectional image of the heterostructure and corresponding chemical analyses. The thickness was measured to be 10 ± 1 nm from the HAADF STEM image shown in Fig. 3(a). The elemental distribution was measured by spectrum imaging from the HAADF signal and EDS spectra. Fig. 3(b) shows a colour-coded map of Cr, Fe and Ni. An O map recorded from the same region reveals local enrichment below and above the Py, at the positions of the Cr and Al layers. In addition, a small amount (<10 at. %) of O was detected (not shown) everywhere in the specimen, as a result of oxidation of the TEM specimen surface. The composition measurement (Fig. 3(c)) indicates that the Ni/Fe at. % ratio is approximately 65/35, which is Ni-poor relative to the nominal permalloy composition ($Ni_{83}Fe_{17}$).

Figs. 1(b–g) show the step-by-step experimental procedure for quantitative magnetic imaging of the Py islands. Fig. 1(b) shows an off-axis electron hologram containing interference fringes that change direction at the positions of the Py islands (Fig. 1(c)). Processing of the off-axis electron holograms was carried out using the Fourier transformation method described in Ref. [20]. Inverse Fourier transformation of a sideband in the Fourier transform of the hologram can be used to provide both an amplitude image (Fig. 1(d)) that contains similar information to that in a conventional bright-field TEM image and a phase shift image. Electrostatic (φ_{el}) and magnetic (φ_{mag}) contributions to the phase shift were separated by performing two consecutive off-axis electron holography experiments from each region of interest. The sample was first tilted to +90° and a vertical magnetic field of 1.5 T was applied using the objective lens of the microscope. The magnetising process was repeated at −90° in order to reverse the magnetic field direction in the islands. The assumption is that their magnetic state stays similar in form but changes direction. After alignment, half of
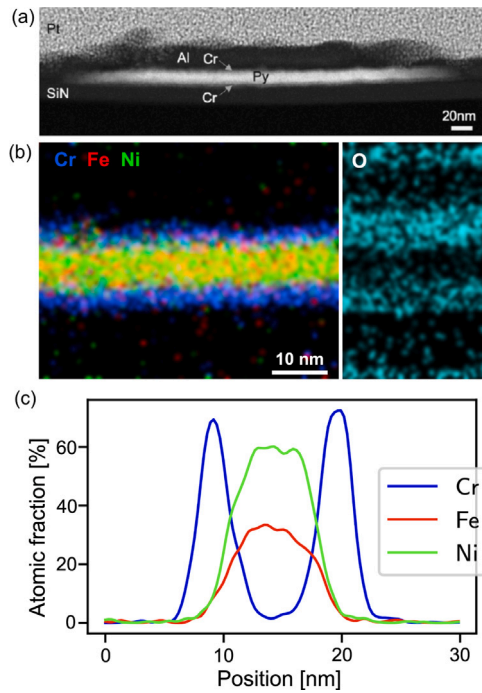
Fig. 3. Structure and chemical composition of the spin ice islands measured in cross-sectional geometry. (a) HAADF STEM image of the layer stack. The Pt is a protective layer deposited during FIB preparation. (b) EDS chemical element maps recorded from the middle of the Py layer showing Cr, Fe, Ni and O distributions. (c) Linescan of the composition across the Py element.

the sum and half of the difference between such pairs of phase images results in φ_{el} and φ_{mag} phase shift maps expressed in radians, as shown in Figs. 1(e,f). A visual representation of the magnetic induction map (Fig. 1(f)), according to Eq. (4), is obtained by evaluating the cosine of a chosen multiple of the magnetic phase shift. The resulting magnetic induction map of the Py islands at remanence shows that the individual islands are in single magnetic domain states, while also revealing the magnetic stray fields both within and at the edges of the array. A closer look at the individual Py islands (inset in Fig. 1(g)) reveals that the magnetic induction curls at the edges of the islands [33], presumably resulting in part from interactions with neighbouring elements.

The experimental magnetic phase shift φ_{mag} obtained from off-axis electron holography experiments (Fig. 1(f)) was used to calculate the projected in-plane magnetic polarisation $\mu_0 M_{xy}$ by applying the MBIR approach. The reconstructed $\mu_0 M_{xy}$ maps correspond to an average of the in-plane components of $\mu_0 M$ in the electron beam direction over the thickness of the Py island. The reconstruction requires identification of the outlines of the Py islands as *a priori* knowledge, given that magnetic material is present only inside the nanomagnets. Fig. 4(a) shows the projected in-plane magnetic polarisation $\mu_0 M_{xy}$ of the Py islands in the chiral ice pattern. The colours define the local magnetic field direction and strength. Small deviations are only observed at the edges of the islands, matching the previous observation made in Fig. 1(g). The distribution of values of measured projected in-plane magnetic polarisation $\mu_0 M_{xy}$ is plotted in Fig. 4(b). The average value of $\mu_0 M_{xy}$ in the Py islands (Fig. 4(a)) is 0.73 ±0.07 T. Values that exceed 1 T are likely to be artefacts resulting from the incorrect local application of a mask around the islands to calculate the magnetisation using the MBIR approach.

Because the magnetic domain structure is sensitive to effects such as the morphology, composition and magnetic history of the system, which are not all known precisely, it is necessary to compare the measurements with micromagnetic simulations to fully understand the experimental results. Fig. 4(c), shows a micromagnetic simulation [34]
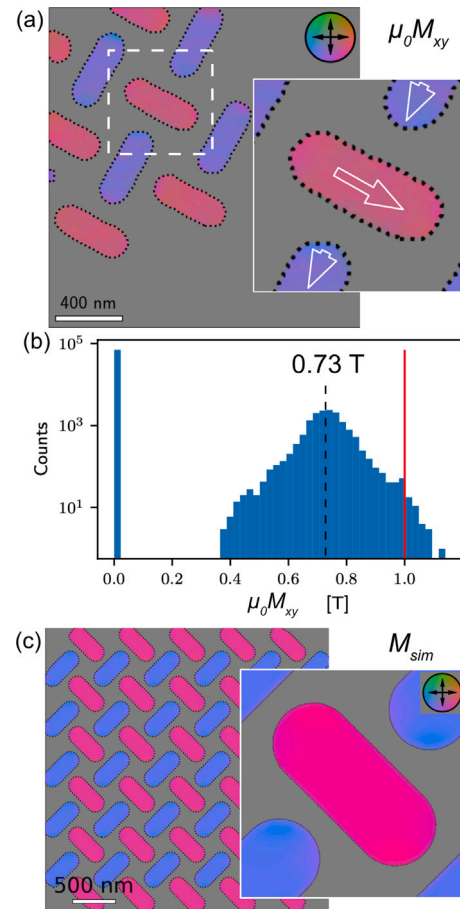

Fig. 4. Reconstruction of the projected in-plane magnetic polarisation $\mu_0 M_{xy}$ using model-based iterative reconstruction. (a) Magnetic polarisation map of the Py islands determined from the experimental magnetic phase shift φ_{mag}. (b) Distribution of measured $\mu_0 M_{xy}$ values in the reconstruction. The average value over all of the islands in (a) is 0.73 T. (c) Micromagnetic simulation of the chiral ice sample. The inset shows a close-up of a single island, revealing parallel magnetisation along its main axis.

of chiral ice islands with an ideal geometry. Remarkably, despite edge imperfections in the patterned structures, oxidation and an uneven distribution of Ni and Fe across the islands, there is very good agreement between the measured (M_{proj}) and simulated (M_{sim}) in-plane magnetisation distributions.

5. Discussion

The projected in-plane magnetisation in a chiral ice sample was reconstructed using MBIR from the experimental magnetic phase shift. Based on the measured specimen thickness, the average value of $\mu_0 M_{xy}$ through the thickness of the islands was determined to be 0.73 T, which is lower than the value of 1 T measured for a 180-nm-thick Py sample deposited under similar conditions [17]. This difference is likely to be due to a combination of different factors. First, the chemical composition of the Py layer was measured to be different from the nominal value ($Ni_{83}Fe_{17}$), with an Fe composition of approximately 35 at.%. Although measurements have shown [35] that the magnetisation of Py increases with Fe content, its magnetisation has also been reported to depend on film thickness and on the structure of the Py [36]. The decrease in magnetisation has been reported to be gradual down to ~20 nm, below which it is more rapid. Depth-sensitive compositional analyses reported in Ref. [36] have revealed the presence of a surface oxide layer, which could explain the observed reduction in

magnetisation. Our chemical composition measurements (Fig. 3) of 10-nm-thick Py islands confirmed the presence of O below and above the Py layer, which may have affected its magnetic properties.

Our micromagnetic simulations suggest that the nanomagnets are too large to reverse through coherent rotation of the magnetisation. Instead, reversal proceeds predominantly through buckling of the magnetisation and magnetic domain wall nucleation. In addition, the magnetisation can reverse through curling and vortex nucleation; this vortex can be stabilised within the nanomagnet. Here, the nucleation of single vortices during switching can be favourable under two conditions: (1) the magnetostatic interaction with neighbouring nanomagnets is weak, such as at the edges of the array and (2) the inversion symmetry of the magnetisation within individual nanomagnets is broken. The second condition is not present in ideally-shaped nanomagnets. However, the fabricated nanomagnet shapes are imperfect, favouring symmetry breaking. Fig. 5 shows magnetic induction maps of a chiral ice sample made of Py islands with a thickness of 18 nm fabricated under the same conditions as the sample described above. This sample was saturated in-plane and small fields (20 and 25 mT) were applied in opposite directions in order to switch the magnetisation. Several Py islands change their magnetic state, supporting magnetic vortices with field lines forming closed loops. The magnetic vortices form randomly in approximately 16% of the islands. The result shown in Fig. 5 was obtained 6 months after deposition, when approximately 7% of the islands formed vortex states during magnetisation reversal. The density of the vortex states may be affected by oxidation of the Py islands after deposition. Future systematic studies of Py oxidation in thin layers and its effect on magnetic properties are required to understand this effect.

6. Summary

The magnetic state of a chiral ice pattern consisting of interacting Py islands was studied quantitatively using off-axis electron holography and model-based reconstruction of the magnetisation. The experimental magnetic induction maps revealed that individual islands are in single domain states. They also show the fine structure of the magnetic field distribution, which contains S-type bending, as well as the magnetic stray field distribution of the array. Based on the measured specimen thickness, the average value of the in-plane magnetic polarisation of the Py islands was measured to be 0.73 T, which is lower than the bulk value (1 T). This reduction is probably due to a degradation of the magnetic properties of the thin Py layer due to oxidation. Moreover, symmetry breaking of the static magnetic structure due to lithographic imperfections (and intermixing), oxidation and inhomogeneous Fe and Ni distributions were found to affect magnetisation reversal in certain nanomagnets. The quantitative magnetic imaging methodology presented in this work has great potential to study the magnetic properties of nanostructures due to its nm-scale spatial resolution and the possibility of also measuring the structure, chemical composition and electronic properties of the same region of the same sample in the TEM. Electron optical phase shift maps of magnetic fields recorded as a function of specimen tilt angle can be used in future studies to reconstruct the magnetic induction field in three dimensions [37], as well as the magnetisation in three dimensions by applying the MBIR method.

CRediT authorship contribution statement

Teresa Weßels: Conceptualization, Investigation, Formal analysis, Methodology, Writing – original draft. **András Kovács:** Conceptualization, Methodology, Writing – original draft. **Sebastian Gliga:** Methodology, Formal analysis. **Simone Finizio:** Resources. **Jan Caron:** Methodology, Software. **Rafal E. Dunin-Borkowski:** Methodology, Funding acquisition, Writing – review & editing.
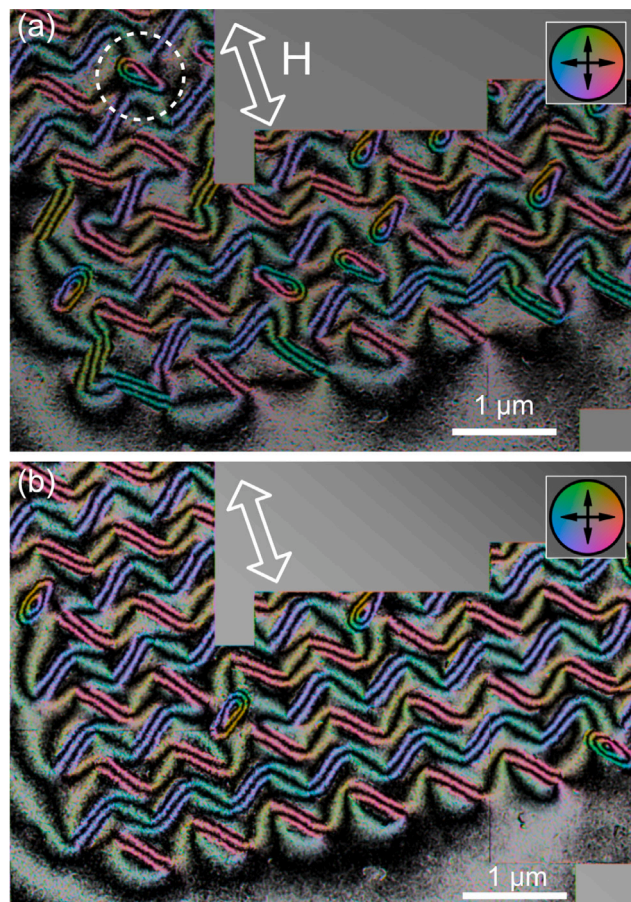

Fig. 5. Magnetic induction maps of a Py chiral ice sample of thickness 18 nm studied 6 months after preparation. A magnetic field (*H*) of (a) 20 and (b) 25 mT was applied in-plane in opposite directions to achieve full saturation before recording the off-axis electron holograms.

Declaration of competing interest

The authors declare that they have no known competing financial interests or personal relationships that could have appeared to influence the work reported in this paper.

Acknowledgements

References

[1] S.H. Skjærvø, C.H. Marrows, R.L. Stamps, L.J. Heyderman, Advances in artificial spin ice, Nat. Rev. Phys. 2 (1) (2020) 13–28, http://dx.doi.org/10.1038/s42254-019-0118-3.

[2] V.M. Parakkat, K. Xie, K.M. Krishnan, Tunable ground state in heterostructured artificial spin ice with exchange bias, Phys. Rev. B 99 (2019) 054429, http://dx.doi.org/10.1103/PhysRevB.99.054429.

[3] S. Gliga, E. Iacocca, O.G. Heinonen, Dynamics of reconfigurable artificial spin ice: Toward magnonic functional materials, APL Mater. 8 (4) (2020) 040911, http://dx.doi.org/10.1063/1.5142705.

[4] M.T. Kaffash, S. Lendinez, M.B. Jungfleisch, Nanomagnonics with artificial spin ice, Phys. Lett. A 402 (2021) 127364, http://dx.doi.org/10.1016/j.physleta.2021.127364.

[5] H. Arava, P.M. Derlet, J. Vijayakumar, J. Cui, N.S. Bingham, A. Kleibert, L.J. Heyderman, Computational logic with square rings of nanomagnets, Nanotechnology 29 (26) (2018) 265205, http://dx.doi.org/10.1088/1361-6528/aabbc3.

[6] J.H. Jensen, G. Tufte, Reservoir computing in artificial spin ice, in: Artificial Life Conference Proceedings, MIT Press, 2020, pp. 376–383, http://dx.doi.org/10.1162/isal_a_00268.

[7] R.F. Wang, C. Nisoli, R.S. Freitas, J. Li, W. McConville, B.J. Cooley, M.S. Lund, N. Samarth, C. Leighton, V.H. Crespi, P. Schiffer, Artificial 'spin ice' in a geometrically frustrated lattice of nanoscale ferromagnetic islands, Nature 439 (7074) (2006) 303–306, http://dx.doi.org/10.1038/nature05607.

[8] S. Gliga, G. Hrkac, C. Donnelly, J. Büchi, A. Kleibert, J. Cui, A. Farhan, E. Kirk, R.V. Chopdekar, Y. Masaki, N.S. Bingham, A. Scholl, R.L. Stamps, L.J. Heyderman, Emergent dynamic chirality in a thermally driven artificial spin ratchet, Nature Mater. 16 (11) (2017) 1106–1111, http://dx.doi.org/10.1038/nmat5007.

[9] Y. Li, G.W. Paterson, G.M. Macauley, F.S. Nascimento, C. Ferguson, S.A. Morley, M.C. Rosamond, E.H. Linfield, D.A. MacLaren, R. Macêdo, C.H. Marrows, S. McVitie, R.L. Stamps, Superferromagnetism and Domain-Wall Topologies in Artificial "Pinwheel" Spin Ice, ACS Nano 13 (2) (2019) 2213–2222, http://dx.doi.org/10.1021/acsnano.8b08884.

[10] M. Wyss, S. Gliga, D. Vasyukov, L. Ceccarelli, G. Romagnoli, J. Cui, A. Kleibert, R.L. Stamps, M. Poggio, Stray-field imaging of a chiral artificial spin ice during magnetization reversal, ACS Nano 13 (12) (2019) 13910–13916, http://dx.doi.org/10.1021/acsnano.9b05428.

[11] X. Cheng, D. Keavney, Studies of nanomagnetism using synchrotron-based x-ray photoemission electron microscopy (X-PEEM), Rep. Progr. Phys. 75 (2) (2012) 026501, http://dx.doi.org/10.1088/0034-4885/75/2/026501.

[12] S. Ladak, D. Read, G. Perkins, L. Cohen, W. Branford, Direct observation of magnetic monopole defects in an artificial spin-ice system, Nat. Phys. 6 (5) (2010) 359–363, http://dx.doi.org/10.1038/nphys1628.

[13] E. Mengotti, L.J. Heyderman, A.F. Rodríguez, F. Nolting, R.V. Hügli, H.-B. Braun, Real-space observation of emergent magnetic monopoles and associated Dirac strings in artificial kagome spin ice, Nat. Phys. 7 (1) (2011) 68–74, http://dx.doi.org/10.1038/nphys1794.

[14] N. Shibata, S.D. Findlay, Y. Matsumoto, Y. Kohno, T. Seki, G. Sánchez-Santolino, Y. Ikuhara, Direct Visualization of Local Electromagnetic Field Structures by Scanning Transmission Electron Microscopy, in: Accounts of Chemical Research, Acc. Chem. Res. 50 (7) (2017) 1502–1512, http://dx.doi.org/10.1021/acs.accounts.7b00123.

[15] R.E. Dunin-Borkowski, A. Kovács, T. Kasama, M.R. McCartney, D.J. Smith, Electron Holography, in: J.C.H. Hawkes (Ed.), Springer Handbook of Microscopy, Springer International Publishing, 2019, pp. 767–818, http://dx.doi.org/10.1007/978-3-030-00069-1_16.

[16] J. Zweck, Imaging of magnetic and electric fields by electron microscopy, J. Phys.: Condens. Matter 28 (40) (2016) 403001, http://dx.doi.org/10.1088/0953-8984/28/40/403001.

[17] S. Finizio, S. Wintz, D. Bracher, E. Kirk, A. Semisalova, J. Förster, K. Zeissler, T. Weßels, M. Weigand, K. Lenz, A. Kleibert, J. Raabe, Thick permalloy films for the imaging of spin texture dynamics in perpendicularly magnetized systems, Phys. Rev. B 98 (2018) 104415, http://dx.doi.org/10.1103/PhysRevB.98.104415.

[18] Ernst Ruska-Centre for Microscopy and Spectroscopy with Eelctrons, Forschungszentrum Jülich and RWTH Aachen, FEI Titan G2 80-200 CREWLEY, J. Large-Scale Res. Facil. 2 (2016) A43, http://dx.doi.org/10.17815/jlsrf-2-68.

[19] A. Kovács, R.E. Dunin-Borkowski, Chapter 2 - Magnetic imaging of nanostructures using off-axis electron holography, in: Handbook of Magnetic Materials, Vol. 27, 2018, pp. 59–153, http://dx.doi.org/10.1016/bs.hmm.2018.09.001.

[20] F. Zheng, A. Kovács, T. Denneulin, J. Caron, T. Weßels, R.E. Dunin-Borkowski, Magnetic field mapping using off-axis electron holography in the transmission electron microscope, J. Vis. Exp. 166 (2020) e61907, http://dx.doi.org/10.3791/61907.

[21] Ernst Ruska-Centre for Microscopy and Spectroscopy with Electrons, Forschungszentrum Jülich and RWTH Aachen, FEI Titan G2 60-300 HOLO, J. Large-Scale Res. Facil. 2 (2016) A44, http://dx.doi.org/10.17815/jlsrf-2-70.

[22] S.L. Chang, C. Dwyer, J. Barthel, C.B. Boothroyd, R.E. Dunin-Borkowski, Performance of a direct detection camera for off-axis electron holography, Ultramicroscopy 161 (2016) 90–97, http://dx.doi.org/10.1016/j.ultramic.2015.09.004.

[23] P. Diehle, A. Kovács, T. Duden, R. Speen, K. Žagar Soderžnik, R.E. Dunin-Borkowski, A cartridge-based turning specimen holder with wireless tilt angle measurement for magnetic induction mapping in the transmission electron microscope, Ultramicroscopy 220 (2021) 113098, http://dx.doi.org/10.1016/j.ultramic.2020.113098.

[24] F. de la Peña, E. Prestat, V.T. Fauske, P. Burdet, T. Furnival, P. Jokubauskas, M. Nord, T. Ostasevicius, K.E. MacArthur, D.N. Johnstone, M. Sarahan, J. Lähnemann, J. Taillon, Hyperspy/Hyperspy: Release v1.6.1, 2020, available at doi:10.5281/zenodo.4294676.

[25] J. Caron, Model-Based Reconstruction of Magnetisation Distributions in Nanostructures from Electron Optical Phase Images (Ph.D Thesis), RWTH Aachen University, 2017.

[26] A. Lubk, Advances in Imaging and Electron Physics, vol. 206, Elsevier, 2018, pp. 15–58, http://dx.doi.org/10.1016/bs.aiep.2018.05.005.

[27] Y. Aharonov, D. Bohm, Significance of Electromagnetic Potentials in the Quantum Theory, Phys. Rev. 115 (1959) 485–491, http://dx.doi.org/10.1103/PhysRev.115.485.

[28] W. Ehrenberg, R. Siday, The refractive index in electron optics and the principles of dynamics, Proc. Phys. Soc. Lond. B 62 (1949) 8–21, http://dx.doi.org/10.1088/0370-1301/62/1/303.

[29] H. Lichte, M. Lehmann, Electron holography: basics and applications, Rep. Progr. Phys. 71 (1) (2007) 016102, http://dx.doi.org/10.1088/0034-4885/71/1/016102.

[30] M. Beleggia, T. Kasama, R.E. Dunin-Borkowski, The quantitative measurements of magnetic moments from phase images of nanoparticles and nanostructures - I. Fundamentals, Ultramicroscopy 110 (2010) 425–432, http://dx.doi.org/10.1016/j.ultramic.2009.10.007.

[31] D. Song, Z.-A. Li, J. Caron, A. Kovács, H. Tian, C. Jin, H. Du, M. Tian, J. Li, J. Zhu, R.E. Dunin-Borkowski, Quantification of Magnetic Surface and Edge States in an FeGe Nanostripe by Off-Axis Electron Holography, Phys. Rev. Lett. 120 (2018) 167204, http://dx.doi.org/10.1103/PhysRevLett.120.167204.

[32] K.M. Krishnan, Fundamentals and Applications of Magnetic Materials, first ed., Oxford University Press, 2016.

[33] C. Phatak, A.K. Petford-Long, O. Heinonen, M. Tanase, M. De Graef, Nanoscale structure of the magnetic induction at monopole defects in artificial spin-ice lattices, Phys. Rev. B 83 (17) (2011) 174431, http://dx.doi.org/10.1103/PhysRevB.83.174431.

[34] A. Kákay, E. Westphal, R. Hertel, Speedup of FEM micromagnetic simulations with graphical processing units, IEEE Trans. Magn. 46 (6) (2010) 2303–2306, http://dx.doi.org/10.1109/TMAG.2010.2048016.

[35] R.D. Tikhonov, A.A. Cheremisinov, Magnetization of Permalloy films, Russ. Microelectron. 46 (2) (2017) 95–104, http://dx.doi.org/10.1134/S106373971702010X.

[36] K. Ounadjela, H. Lefakis, V. Speriousu, C. Hwang, P. Alexopoulos, Effect of surface composition observed by Auger electron spectroscopy on magnetization and magnetostriction of NiFe and NiFeRh thin films, J. Appl. Phys. 65 (3) (1989) 1230–1233, http://dx.doi.org/10.1063/1.343014.

[37] D. Wolf, N. Biziere, S. Sturm, D. Reyes, T. Wade, T. Niermann, J. Krehl, B. Warot-Fonrose, B. Büchner, E. Snoeck, C. Gatel, A. Lubk, Holographic vector field electron tomography of three-dimensional nanomagnets, Commun. Phys. 2 (2019) 87, http://dx.doi.org/10.1038/s42005-019-0187-8.